



Full paper

Carbon-pore-sheathed cobalt nanoseeds: An exceptional and durable bifunctional catalyst for zinc-air batteries

Zhenyu Xing^{a,b,1}, Ya-Ping Deng^{a,1}, Serubbabel Sy^a, Guoqiang Tan^c, Aiju Li^b, Jingde Li^a, Yue Niu^a, Na Li^d, Dong Su^d, Jun Lu^c, Zhongwei Chen^{a,*}

^a Department of Chemical Engineering, Waterloo Institute for Nanotechnology, Waterloo Institute for Sustainable Energy, University of Waterloo, 200 University Avenue W, Waterloo, Ontario, N2L 3G1, Canada

^b Department of Chemistry, South China Normal University, Guangzhou, 510006, PR China

^c Chemical Sciences and Engineering Division, Argonne National Laboratory, Argonne, Illinois, 60439, USA

^d Center for Functional Nanomaterials, Brookhaven National Laboratory, Upton, NY, 11973, USA

ARTICLE INFO

Keywords:

Zinc-air batteries
Bifunctional catalyst
Carbon pore confinement
Carbon defects
Durability

ABSTRACT

Exceptional and durable catalysts for Zinc-air batteries are plagued by nanoparticle agglomeration. As a proof-of-concept, we designed carbon-pore-sheathed cobalt nanoseeds by loading cobalt nanoparticles into N-doped defective carbon pores. Introduced N-doping, Co–N–C bond and graphitic/graphenic carbon defects endow the catalyst with exceptional catalytic activity. Most importantly, the design of Co confined within carbon pores effectively solved the dilemma of nanomaterial stability. By balancing the high catalytic activity and stable cyclability, this unique catalyst is among the outstanding bifunctional catalysts, with a high ORR half-wave potential of 0.847 V and a low OER potential at 10 mA/cm² of 1.593 V. As demonstrated in the full cell, a peak power density of 135 mW/cm² at a current density of 200 mA/cm² and 450 h of stable cycling performance without fading at a current density of 30 mA/cm² was delivered.

1. Introduction

Realizing the plight of fossil fuel depletion and pollution, researchers have started to recast their focus onto alternative energy sources [1–3]. Unfortunately, an effective energy storage system for portable electronics and electric vehicles is still lacking albeit Li-ion batteries (LIBs) have gained a dominating market share after intensive investigations [4–9]. Notably, the energy density of 250 Wh/kg from LIBs cannot relieve the range anxiety of electric vehicles [10]. Therefore, researchers begin to divert their efforts towards metal-air batteries, which possess much higher energy densities [11–14]. Among various metal-air batteries, Zn-air battery is the one of the most promising candidates to replace LIBs due to its usage of an environmentally-friendly, Zn-metal anode, which is also available abundantly and low in cost [15–20]. Nevertheless, following issues plague Zn-air batteries, including clogged gas diffusion layer by carbonate salts from ambient CO₂, labile separator in strong basic solution, Zn dendrite formation and self-discharge due to H₂ evolution. Compared with above issues, the most serious obstacle lies in the cathode side. Zn-air batteries undergo drawbacks similar to many other metal-air batteries, which

involve high overpotentials by cause of sluggish ORR/OER kinetics and deteriorated catalytic activity after long cycling [21].

An ideal structure should possess a facile electron-transfer network and an unhindered electrolyte/gas-diffusion artery to obtain the highest possible catalytic activity [22,23]. Apparently, nanonization is thereby an optimal strategy to fulfill the previously mentioned requirements, i.e. reducing the particle size to nanoscale will expose more active crystal facets, resulting in a superior catalytic activity to that of its bulk phase [24–28]. Despite the tremendous advantage towards nanonization, an irremissible disadvantage is hidden in its stability. In particular, nanoparticles tend to agglomerate in the post-treatment and long cycling tests, which thereby deteriorate the catalytic activity. Recently, dispersing nanoparticles over porous carbon host offers an effective strategy to solve the agglomeration issue of nanoparticles [29–33]. However, the carbon host function can be further explored based on the confinement effect of carbon pores.

Herein as a proof-of-concept, we designed carbon-pore-sheathed cobalt nanoseeds for Zn-air batteries by loading cobalt (Co) nanoparticles into N-doped defective carbon pores, as illustrated in Fig. 1. During nitridation and carbothermic reduction of Co-hydrolyzed

* Corresponding author.

E-mail address: zhwchen@uwaterloo.ca (Z. Chen).

¹ These authors equally contributed to the paper.

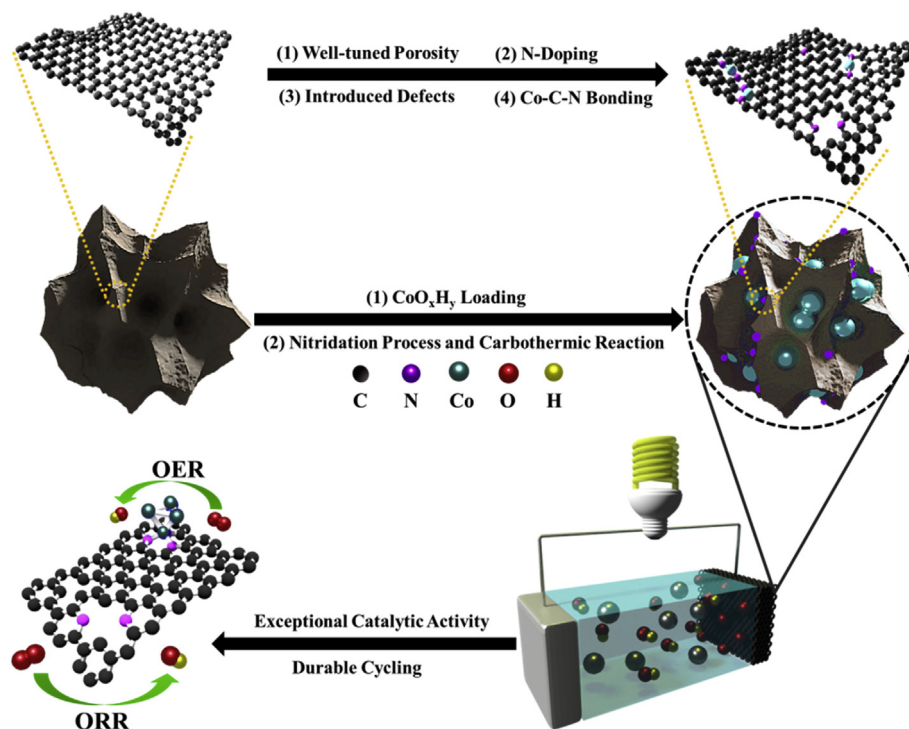


Fig. 1. Preparation and structure of KJ-Co-H as a bifunctional catalyst used in a Zn-Air battery.

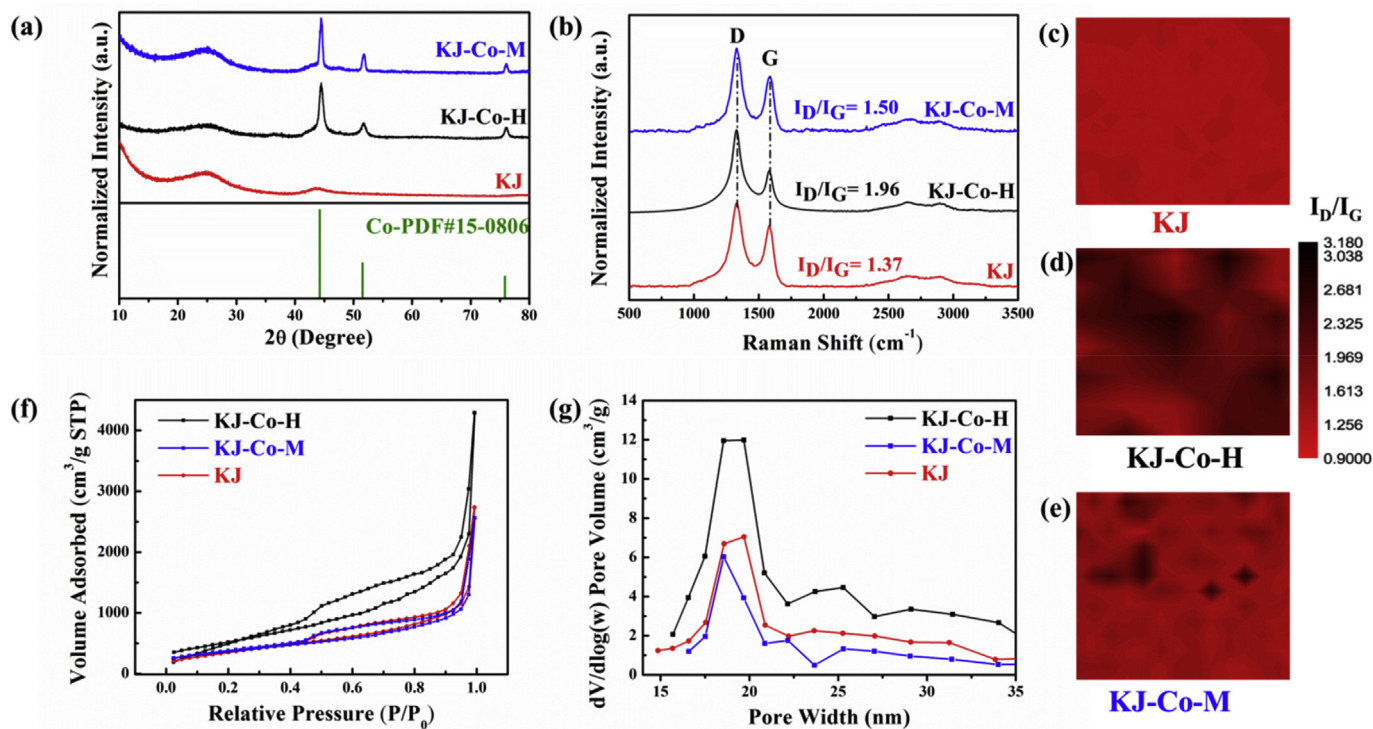


Fig. 2. (a) XRD patterns of KJ, KJ-Co-H, and KJ-Co-M. (b) Raman spectra of KJ, KJ-Co-H, and KJ-Co-M. Contour plots of I_D/I_G from the Raman mapping with a $200\mu\text{m}\times 200\mu\text{m}$ scan area for (c) KJ, (d) KJ-Co-H, and (e) KJ-Co-M. (f) Nitrogen sorption isotherms of KJ, KJ-Co-H, and KJ-Co-M. (g) Corresponding pore size distribution of KJ, KJ-Co-H, and KJ-Co-M.

product, introduced N-doping, Co-N-C bond and graphitic/graphenic carbon defects endow this catalysts with exceptional catalytic activity. Most importantly, the design of Co confined within carbon pores effectively solved revalent dilemma with nanomaterial stability. By balancing the high catalytic activity and stable cyclability, this unique catalyst delivered a high ORR half-wave potential of 0.847 V and a low

OER potential at $10\text{ mA}/\text{cm}^2$ of 1.593 V, which is among the outstanding bifunctional catalysts. A full cell delivers a peak power density of $135\text{ mW}/\text{cm}^2$ at a current density of $200\text{ mA}/\text{cm}^2$, and 450 h of stable cycling performance without fading at a current density of $30\text{ mA}/\text{cm}^2$.

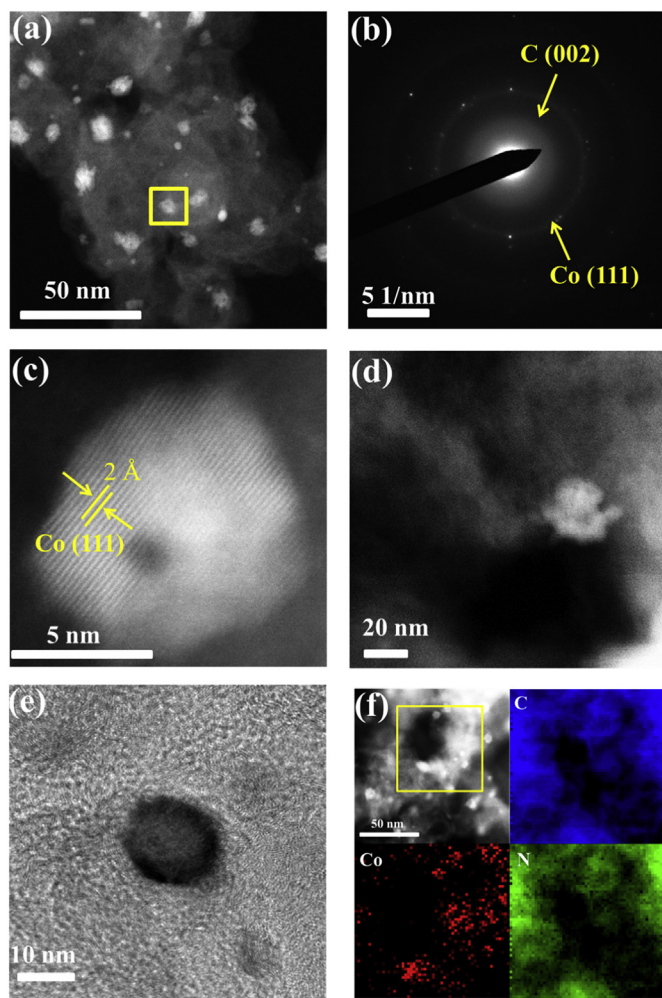


Fig. 3. TEM images of KJ-Co-H in the dark field (a), (c), (d) and bright field (e). (b) SAED of KJ-Co-H. (f) EELS mappings of carbon, cobalt, nitrogen signals from the yellow box.

2. Experimental section

2.1. Preparation of KJ-Co-H

KJ-600 carbon was purchased from MTI Cooperation, China. For KJ-Co-H, the KJ carbon with absorbed water vapor under ammonium gas flow was subsequently immersed into saturated cobalt (II) acetylacetonate/ethyl acetate solution for 6 h. Afterwards, the filtrated sample was heated in the tube furnace under ammonium flow (60 SCCM) at 850 °C for 1 h.

2.2. Preparation of KJ-Co-M

As a control, KJ-600 was firstly chemically mixed with Co_3O_4 with the same Co/C ratio as KJ-Co-H. Then, the as-prepared sample was heated in the tube furnace under ammonium flow at 850 °C for 1 h.

2.3. Characterization methods

A MiniFlex 600 Rigaku Diffractometer with $\text{Cu K}\alpha$ irradiation ($\lambda = 1.5406 \text{ \AA}$) were used to record XRD patterns. Raman spectra were collected by WITec alpha300R with a 532 nm solid laser as an excitation source. Transmission electron microscopy (TEM) and high resolution transmission electron microscopy (HRTEM) images were collected by TEM (JEOL 2010F TEM/STEM). Brunauer–Emmett–Teller (BET)

tests and related pore size distribution analysis were performed on Autosorb iQ Station 1. A Thermo Scientific K-Alpha spectrometer is employed to obtain XPS measurements.

2.4. Electrochemical measurement

The oxygen electrocatalytic performance was measured in a three-electrode configuration on a Biologic VSP 300 electrochemical workstation and rotation speed controller (RDE, Pine Instrument Co., AFMSRCE). A glassy carbon electrode (GCE, 0.196 cm^2) was used as the working electrode and a graphitic rod as the counter electrode. All the results were obtained with reference to a saturated calomel electrode (SCE) followed by the calibration to the reversible hydrogen electrode (RHE) based on the Nernst equation: $E_{\text{RHE}} = E_{\text{SCE}} + 0.059 \times \text{pH} + 0.241$. 0.1 M KOH solution was used as the electrolyte with a resistance of $40 \ \Omega$ for iR-compensation. Oxygen gas was continuously bubbled during the ORR and OER tests to confirm the oxygen saturation. The catalyst ink was prepared by dispersing 2 mg as-prepared catalyst in 400 μL 0.1 wt% Nafion ethanol solution under ultrasonication for about 1 h. The commercial Pt/C with 20 wt% Pt and Ir/C with 20 wt% Ir were also dispersed with the same procedure as respective ORR and OER benchmarks. Afterwards, 8 μL ink was pipetted onto the GCE. The calculation of electron transfer number per oxygen molecule is based on the Koutecky-Levich (K-L) equation: $\frac{1}{j} = \frac{1}{j_k} + \frac{1}{B\omega^{1/2}}$, where j_k is the kinetic current and B is Levich slope: $B = 0.2nFD_0^{2/3}C_0\nu^{-1/6}$; F is the Faraday constant of 96485 C/mol , D_0 is the oxygen diffusion coefficient of $1.9 \times 10^{-5} \text{ cm}^2 \text{ s}^{-1}$, C_0 is the oxygen saturated concentration of $1.1 \times 10^{-6} \text{ mol cm}^{-3}$ in 0.1 M KOH, ν is the kinematic viscosity of $0.01 \text{ cm}^2 \text{ s}^{-1}$ in 0.1 M KOH.

2.5. Full cell fabrication

The single-cell Zn-air battery tests were carried out on plastic prototypes containing catalyst-sprayed gas diffusion layer (GDL, SGL Carbon 39 BC, Ion Power Inc) with a catalyst loading of 1 mg cm^{-2} as the air electrode and a polished zinc plate as the anode. After, the solution of 6 M KOH and 0.2 M $\text{Zn}(\text{CH}_3\text{COO})_2$ was filled into the prototypes as electrolyte. The mixture of commercial Pt/C and Ir/C at an equal mass ratio was also sprayed on GDL with the same fabrication process as the performance benchmark. The galvanostatic rechargeable tests were recorded on a Land battery tester (LAND-CT2001A, Land Electronic Co., Ltd., Wuhan) under ambient conditions.

2.6. DFT calculation and computational modeling

The computational simulations were conducted by Vienna ab-initio simulation package (VASP), which applied projector augmented wave (PAW) pseudo-potentials, to reveal the interaction between the nuclei and its electrons via density functional theory (DFT). Within the generalized gradient approximation (GGA), the Perdew-Burke-Ernzerhof (PBE) equation was used to describe the electronic exchange and correlation effects. Firstly in this work, a graphene supercell with 5×4 hexagon units was built. Then nitrogen elements were doped onto the single-layer graphene to obtain a defect-rich substrate. Afterwards, an optimized cobalt cluster was anchored onto the substrate, which was treated as the model of the catalyst. The periodic boundary conditions were set up along the x-axis with a vacuum layer of 15 \AA to enable an infinite tape in the model. Furthermore, the lattice parameter of the model was $20.0 \text{ \AA} \times 12.3 \text{ \AA} \times 12.3 \text{ \AA}$, within which the relaxed graphene piece fitted. In order to investigate the edge effect, oxygen reduction reaction (ORR) and oxygen evolution reaction (OER) on as-built single-layer graphene, free space was created in the models along y- and z-direction.

Brillouin zone, K-point mesh was set up as a $2 \times 2 \times 1$ grid making a gamma point centered within Monkhorst Pack Scheme. The

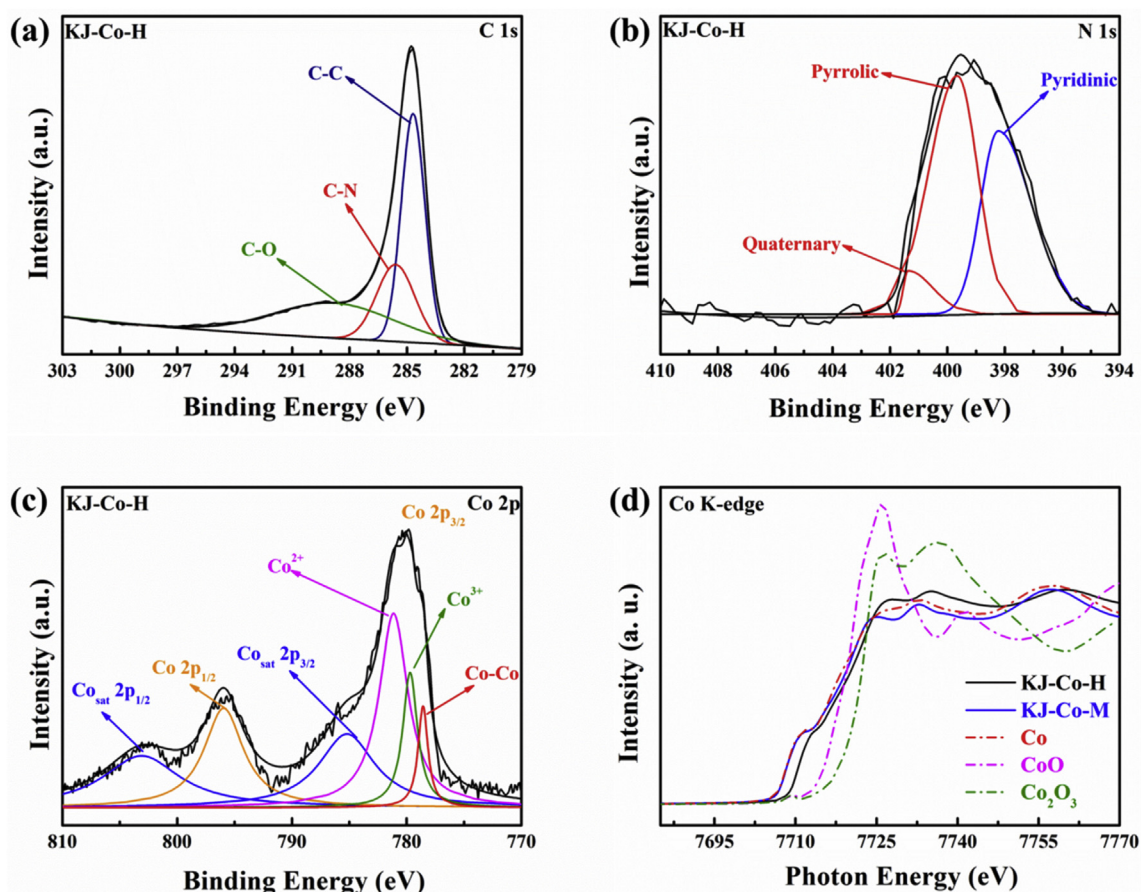


Fig. 4. (a) XPS C1s spectra of KJ-Co-H. (b) XPS N1s spectra of KJ-Co-H. (c) XPS Co 2p spectra of KJ-Co-H. (d) Co K-edge XANES spectra of KJ-Co-H.

simulation was run with a setup of INCAR file. The maximum number of ionic steps was set to 500, and the break condition of the electronic SC-loop was 1.0×10^{-5} eV and 400 eV as the cutOff energy. All the simulations were two-step processes, including the geometrical optimization and static calculation. The structure of the model was fully relaxed during the geometrical optimization process to simulate all the atoms sitting at the point with the total minimum energy. For the calculation process, the adsorption of O^* and OH^* onto the catalyst surface were replicated, thus the adsorption energy at each element step of the ORR/OER could be evaluated.

3. Results and discussion

X-ray diffraction (XRD) measurement was used for the phase analysis. The carbon host KJ-600 and Co-embedded KJ-600 from hydrolysis are denoted as KJ and KJ-Co-H in the following sections, respectively. As a control, a Co/KJ-600 composite with same amount of Co content was also prepared from the mixture of KJ-600 and cobaltous oxide after the ammonium treatment at the same condition, which we will refer to as KJ-Co-M. Compared with the KJ XRD pattern in Fig. 2a, three newly formed peaks of KJ-Co-H were indexed to metallic Co with a cubic structure of space group Fm3m (225), indicating that the cobalt precursor after hydrolysis was reduced to Co. The Co crystallite size along (111) direction was calculated to be 12 nm via the Scherrer equation. Unexpectedly, such small nanoparticles were maintained after a heat treatment of up to 800 °C. Based on speculation, this phenomenon should be attributed to the carbon pore confinement effect, which prevents the Co nanoparticles from agglomerating even under high temperatures. In addition, a typical carbon (002) peak, around 23.7° , broadened and its intensity decreased significantly. According to the Scherrer equation, a coherence length L_c , along (002) direction of the

carbon host, decreased from 1.98 nm to 1.35 nm. This change suggested that the graphitic crystallinity was dramatically weakened, and numerous defects along (002) direction were generated, correspondingly [34]. Different from KJ-Co-H, the Co crystallite size of KJ-Co-M along (111) direction was large and up to 22.5 nm. Moreover, the carbon (002) peak of KJ-Co-M remained similar to that of KJ. This discrepancy between KJ-Co-H and KJ-Co-M could be ascribed to the different circumstances associated with the carbothermic reduction reaction. Based on the synthesis steps, the hydrolysis products of KJ-Co-H were loaded into the carbon pores, while those of KJ-Co-M were mechanically mixed with carbon host. Therefore, KJ-Co-H provided numerous *in situ*, carbothermic reaction sites for the generation of defects along the c-axis, which was far more than that of KJ-Co-M [35].

Aside from XRD results, the defect information of carbon host was also confirmed by L_a from Raman analysis. As shown in Fig. 2b, characteristic carbon D-bands located at 1340 cm^{-1} and G-bands located at 1580 cm^{-1} were assigned to defective C_6 ring with A_{2g} vibration, and sp^2 carbon with E_{2g} vibration, respectively [36]. According to I_D/I_G ratios of 1.96 for KJ-Co-H and 1.50 for KJ-Co-M, more defects were introduced among the *ab* plane for KJ-Co-H than KJ-Co-M. To compare the graphenic feature qualitatively, the following equation was employed to calculate the graphenic domain size L_a (coherence length along *ab* plane):

$$L_a(\text{nm}) = (2.4 \cdot 10^{-10}) \cdot \lambda_{nm}^4 \left(\frac{I_G}{I_D} \right)$$

Here, λ is the Raman laser wavelength [37,38]. As calculated, the graphenic domain size L_a of KJ, KJ-Co-H and KJ-Co-M was approximately 14.1 nm, 9.8 nm and 12.8 nm, respectively. Albeit minimal, but when compared with KJ, the graphenic domain size L_a of KJ-Co-H

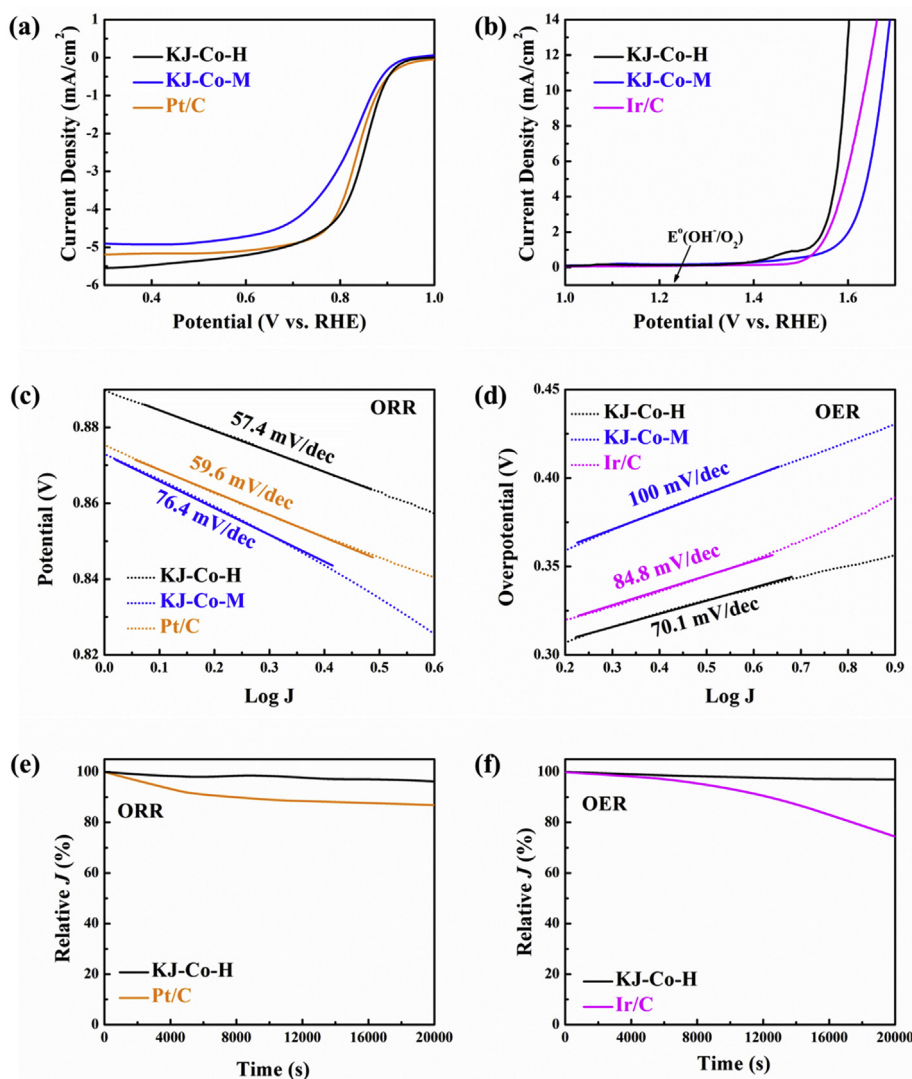


Fig. 5. (a) ORR polarization curves of Pt/C, KJ-Co-H and KJ-Co-M at a rotating speed of 1600 rpm. (b) OER polarization curves of Ir/C, KJ-Co-H and KJ-Co-M at a rotating speed of 1600 rpm. (c) ORR Tafel plots of Pt/C, KJ-Co-H and KJ-Co-M. (d) OER Tafel plots of Ir/C, KJ-Co-H and KJ-Co-M. Stability studies on the half-cell reactions (e) ORR and (f) OER assessed by chronoamperometric measurements at a given constant potential.

decreased significantly, indicating many defects among the *ab* plane were generated *in situ*. To confirm this phenomenon on a larger scope, Raman mapping was conducted on a $200\ \mu\text{m} \times 200\ \mu\text{m}$ area spanning 400 points. From the obtained contour plots the color depth of the vertical profiles represent the intensity ratio of D band vs. G band, while the horizontal plane correspond to the actual scanning area. Additionally on the scale bar, the darker the red hue, the greater the I_D/I_G ratio is, which in turn corresponds to the increased existence of defects. As shown in Fig. 2c, the bright red plane is indicative of the small amount of defects in KJ, i.e. a low I_D/I_G ratio, however, many black spots appeared in Fig. 2d and e for KJ-Co-H and KJ-Co-M respectively. This discrepancy was due to the different carbothermic reduction sites as discussed previously; since the cobalt hydrolysis products were loaded into the carbon pores of KJ-Co-H, there was limited contact between the cobalt precursor and carbon host for KJ-Co-M. The Raman mapping results affirmed that more graphenic defects were generated in KJ-Co-H than KJ-Co-M.

Corroborating the XRD and Raman results, we can conclude that plenty of defects were introduced along the *c*-axis and *ab* plane within KJ-Co-H, resulting from the *in-situ* carbothermic reduction of the cobalt hydrolysis product. This conclusion was further confirmed by the porosity measurement with a N_2 adsorption/desorption. As revealed by

BET results, the surface area of KJ was about $1302\ \text{m}^2/\text{g}$ and its related pore volume was approximately $4.1\ \text{cm}^3/\text{g}$. The corresponding adsorption/desorption curves in Fig. 2f suggest a characteristic IV isotherm with a hysteresis in the medium pressure range. Moreover, a peak at 19 nm in Fig. 2g indicates a very narrow pore size distribution (PSD) by the Barrett-Joyner-Halenda (BJH) method. After the carbothermic reduction of the cobalt hydrolysis product, the surface area and pore volume of KJ-Co-H increased to $1917\ \text{m}^2/\text{g}$ and $6.2\ \text{cm}^3/\text{g}$, despite a heavier Co with a loading of 11 wt% was introduced. This result was further supported by the increased hysteresis area in Fig. 2f and pore volume in Fig. 2g. The increased surface area and enlarged pore volume of KJ-Co-H should be attributed to carbon atom oxidation around cobalt hydrolysis products during the carbothermic reduction. Unlike KJ-Co-H, KJ-Co-M showed a similar isotherm hysteresis curve and PSD to that of KJ. Without a Co precursor loaded into the carbon pores, the mechanical mixing did not provide enough carbothermic reaction sites to etch the carbon host.

Accompanying XRD, Raman and BET results highlighted the carbon host defects and pore-loaded aspects of KJ-Co-H, but these conclusions were drawn implicitly. Therefore, explicit evidence can be attained from TEM, coupled with selected area electron diffraction (SAED) and electron energy loss spectroscopy (EELS) mapping. As shown in Fig. 3a,

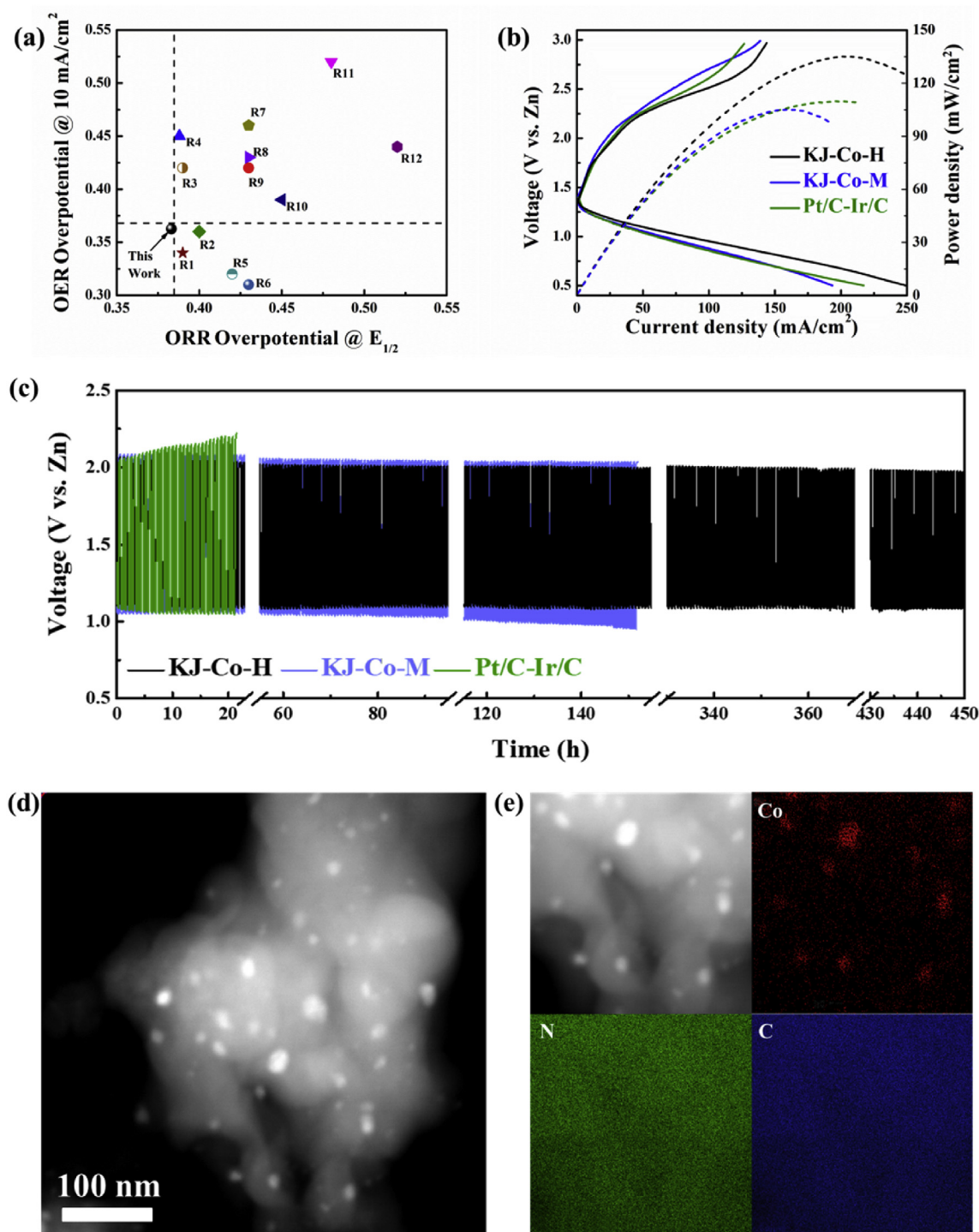


Fig. 6. (a) Comparison of the ORR and OER overpotentials between this work and other published results. Detailed reference data R1-R11 is summarized into Table S3. (b) Polarization and power density curves of Zn – air batteries for Pt/C-Ir/C, KJ-Co-H and KJ-Co-M. (c) Galvanostatic discharge and charge cycling stability of Zn-air battery at a current density of 30 mA cm² with 20 min discharge and 20 min charge. (d) TEM image of KJ-Co-H after 450 h' cycle. (e) HAADF element mapping of KJ-Co-H after 450 h' cycle.

the white nanoparticles were dispersed uniformly over the black host. Based on the cobalt and carbon signals from EELS mapping in Fig. 3f, we can conclude that the distribution of Co nanoparticles on the carbon host was very homogenous. In the corresponding SAED pattern, the well resolved diffraction ring in Fig. 3b was indexed to the Co (111) crystal plane with a d-spacing around 2 Å as shown in Fig. 3c, which is from the enlarged yellow box in Fig. 3a. This isotropic feature confirmed the polynanocrystalline structure of nanoscale Co particles,

agreeing with the calculated crystallite size from the XRD results. Through a higher resolution, the explicit evidence of pore-loaded Co-nanoparticles was presented by HRTEM (Fig. 3d), as a complementary corroboration to the aforementioned BET PSD results. Moreover, the newly-generated carbon defects via carbothermic reduction were also captured in Fig. 3e, if comparing the short and sparse carbon lattice fringes around the Co nanoparticles against the long and dense lattice fringes of KJ in Fig. S1. This distinct contrast correlates the decreased

coherence length, L_c , from the XRD patterns, and the constricted domain size, L_d , from the Raman spectra.

Hitherto, the KJ-Co-H structure, of Co nanoparticles loaded in the defective carbon pores, has been confirmed by XRD, Raman, BET and TEM measurements. Nevertheless, specific chemical bonding states still remain unknown despite EELS mapping providing general elemental confirmation and distribution. To further excavate the bonding information of KJ-Co-H, X-ray photoelectron spectroscopy (XPS) was employed. In agreement with EELS results, the XPS survey attested to the existence of Co, O, N and C in Fig. S2. Under a higher resolution, three deconvoluted subpeaks from C 1s peak in Fig. 4a, located at 284.6 eV, 285.6 eV and 288.8 eV, was identified as C–C, C–N and C–O peak, respectively [39]. The existence of the C–N bonds demonstrated the successful substitution of carbon atoms by N-doping in the carbon lattice network. N-doping has proven effective in altering the local electron density of carbon networks, especially different N-doping types exert disparate influences. As shown in Fig. 4b, the N 1s peak was deconvoluted into three peaks, corresponding to pyridinic N (398.2 eV), pyrrolic N (399.9 eV) and quaternary N (401.3 eV) [40]. Apart from pyrrolic N and quaternary N, pyridinic N was always connected to the metal atom, forming the active catalytic site. To detect whether the Co–N–C bond exists, the Co 2p peak was also deconvoluted in Fig. 4c. The subpeaks located at 803.1 eV and 785.2 eV were assigned to satellite peak $\text{Co}_{\text{sat}} 2p_{1/2}$ and $\text{Co}_{\text{sat}} 2p_{3/2}$, respectively. Apart from the main peak $\text{Co} 2p_{1/2}$ at 795.9 eV, more attention was directed on the other main peak $\text{Co} 2p_{3/2}$ at 780.5 eV. The confirmed Co–Co bond by the peak at 778.5 eV agreed well with the metallic cobalt phase from XRD results. Besides the Co–Co bond, the existence of Co–N–C bond, which connects pyridinic N and metal cations, is confirmed by Co^{2+} (779.7 eV) and Co^{3+} (781.1 eV) peaks with 88.1% peak area of $\text{Co} 2p_{3/2}$ main peak. Compared with KJ-Co-H, the possibility of Co–N–C bond formation in KJ-Co-M dramatically decreased, as proved by 35.2% $\text{Co}^{2+}/\text{Co}^{3+}$ total peak area in Fig. S3.

Finally, the existence of a Co–N–C bond was strongly supported by X-ray absorption near edge structure (XANES), a much more powerful tool to study atom coordination environment in a bulk phase, as compared to XPS. As shown in Fig. 4d, the edge position of KJ-Co-H was among the references of Co foil, CoO and Co_2O_3 , indicating the actual cobalt oxidation state of KJ-Co-H was between 0 and $2+$. The reason to explain the above positive cobalt oxidation state can be seen in the bond formed between Co and N, where electron pairs leaning to the N nucleus. To contrast, there was only a slight shift of curve position for KJ-Co-M, due to the very weak Co–N–C bonds. Supplementary to the edge position, the Co–N–C bond was also confirmed by the peak area after the edge jump, which is positively correlated to the vacancy number [41]. With N accepting donated electrons from Co, there would be more vacancies generated in the Co $(n+1)p$ and nd orbitals, leading to a higher peak area for KJ-Co-H in Fig. 4d, as compared with Co foil.

Here, we have demonstrated that Co nanoparticles were loaded into the N-doped, enlarged, and defective carbon pores via strong Co–N–C bonds. All these features potentially suggest KJ-Co-H as an exceptional catalyst for Zn-air batteries. To affirm this claim, we conducted the following electrochemical tests. ORR catalytic activity was first measured via a rotating disk electrode (RDE) in 0.1 M O_2 -saturated KOH solution. As linear sweep voltammetry (LSV) in Fig. S4a and Fig. S4c show, polarization curves of KJ-Co-H and KJ-Co-M demonstrated typical diffusion-limited currents at low potentials. The nearly-parallel curves in the low potential range under different rotating speeds suggest a first-order reaction kinetic vs. O_2 concentration. Further deriving from LSV curves at various potentials through the Koutecky–Levich equation, K-L curves were plotted in Fig. S4b and Fig. S4d. As it is known, the slope, which is the ratio of the inverse current density to the inverse of the square root of the rotation speed, represent the electron transfer number of ORR. Both KJ-Co-H and KJ-Co-M showed similar four-electron ORR process, indicating fast kinetics exhibited over the whole ORR potential range. However, the superiority of KJ-Co-H to KJ-

Co-M was distinguished in Fig. 5. As the polarization curves at 1600 rpm show, the onset potential of KJ-Co-H is around 0.938 V, much higher than that of KJ-Co-M at 0.925 V. As for the half-wave potential, $E_{1/2}$, KJ-Co-H possessed a significant advantage over KJ-Co-M. The $E_{1/2}$ of KJ-Co-H was 0.847 V, 31 mV higher than KJ-Co-M. Notably, the $E_{1/2}$ of KJ-Co-H was even 12 mV higher than that of a commercial Pt/C catalyst. Additionally, the diffusion-limited current of KJ-Co-H was about -5.353 mA/cm^2 , far higher than -4.873 mA/cm^2 of KJ-Co-M and -5.160 mA/cm^2 of commercial Pt/C catalyst. This comparison indicated a more favorable thermodynamic behavior of KJ-Co-H. In line with the high onset potential and high half-wave potential from a kinetics perspective, the superior ORR activity of KJ-Co-H was also confirmed by the Tafel slope after mass transport correction in Fig. 5c. In the mixed kinetic–diffusion-controlled region, the Tafel slope of KJ-Co-H was 57.4 mV/dec, outperforming 59.6 mV/dec of Pt/C and 76.4 mV/dec of KJ-Co-M. In summary, all the preceding results points toward the superior ORR activity of KJ-Co-H, in contrast to KJ-Co-M, and even the commercial Pt/C catalyst; the reasons of which are revealed in the following aspects. Firstly, the widened pore volume from the carbothermic reaction enhanced the ORR kinetics by facilitating O_2 and OH^- diffusion. Secondly, the Co nanoparticles and carbon host, with its increased surface area, offered numerous reaction active sites. Most importantly, *in situ* generated carbon defects during the carbothermic reaction and newly formed Co–N–C bonds in the nitridation process play vital roles in the advanced ORR activity. To further confirm this hypothesis, we conducted first-principles calculations by using density functional theory (DFT) method. After filtering unseasonable values of O^* adsorption energy, possible structures of ORR active sites with O^* adsorption for KJ-Co-H and KJ-Co-M were shown in Fig. S5 and Fig. S6, and corresponding O^* adsorption energies were summarized into Table S1. We can find that KJ-Co-H contains doped-N, Co–N–C bonds and carbon defects as the active sites while KJ-Co-M only has Co–N–C bonds and planar carbon as the active sites. Specifically, O^* adsorption energies of the active sites in KJ-Co-H are lower than those of same types in KJ-Co-M. To give a direct viewing, O^* adsorption energies of the active sites are plotted in Fig. S7a, and their average values are represented by the loops. Compared with -6.77 eV of KJ-Co-M, the average O^* adsorption energies of KJ-Co-H are only -4.93 eV . According to Sabatier effect, too strong adsorption will lead active sites fully covered by reaction intermediates, impeding consequent elementary reactions. Therefore, KJ-Co-M possessed a much higher ORR overpotential than KJ-Co-H. Moreover, this result also agrees with a well-established theoretical model that a lower O^* adsorption energy contributes to a higher reaction activity [42]. Based on above analysis, we confirmed the hypotheses that generated carbon defects, Co–N–C bonds and doped-N in carbothermic reaction/nitridation process are crucial for the superior ORR activity of KJ-Co-H.

Complementary to ORR, OER was also an equipollent aspect in determining the Zn-air battery performance. As shown in Fig. 5b, OER polarization curves were obtained in 0.1 M O_2 -saturated KOH solution at 1600 rpm. Evidently, there was a bump around 1.47 V for KJ-Co-H, which can be attributed to the oxidation of Co nanoparticle. Similar to KJ-Co-H, a bump also appeared in the polarization curve of KJ-Co-M. However, the bump location upshifted. This discrepancy was due to a better contact between Co nanoparticles and the carbon host of KJ-Co-H, facilitating quicker electron transfer. At a current density of 10 mA/cm^2 , the potential of KJ-Co-H was about 1.593 V, 78 mV lower than that of KJ-Co-M. This value was also 42 mV lower than that of commercial Ir/C catalyst. The corresponding Tafel slope in Fig. 5d further confirmed the superior OER kinetics for KJ-Co-H. Based on the calculations, the Tafel slope of KJ-Co-H is 70.1 mV/dec, much lower than 84.8 mV/dec of commercial Ir/C catalyst and 100 mV/dec of KJ-Co-M. The superior OER catalytic activity of KJ-Co-H can be accredited to the enlarged pore volume as previously discussed in the BET characterization, which contributes to a faster O_2 and OH^- diffusion. Moreover, delocalized electron distribution over the carbon ring network, by the

formation of defects and Co–N bonding induction, facilitated the OH[−] adsorption in the rate-determining step and subsequent electron acceptance. The synergistic effects from the unique structural design endorsed this noteworthy OER activity. Similar to ORR, we also made an attempt to identify possible OER active sites by first-principles calculations with DFT method. Based on the adsorption energies of OH* summarized in Table S2 and corresponding structures in Fig. S8, the active OER sites are Co atoms and carbon defects for KJ-Co-H. In contrast, KJ-Co-M only contains Co atoms in Fig. S9 as active sites. In addition, average OH* adsorption energy is -3.31 eV for KJ-Co-H, much smaller than of -5.01 eV for KJ-Co-M. As discussed above, too strong adsorption of reaction intermediate will impede following elementary reaction, thus increasing OER overpotential as shown in Fig. S7b. Therefore, we identified possible OER active sites of KJ-Co-H as Co atoms and carbon defects, which are in line with above OER superiority analysis.

Comparing the ORR/OER overpotential of KJ-Co-H with other published results in Fig. 6a and detailed information in Table S3, there is no doubt that our results represent the state-of-the-art design. Thus a single-cell Zn-air battery, as shown in Fig. 1, was assembled to assess the practical application. The single-cell test was conducted under ambient air atmosphere with 6 M KOH and 0.2 M Zn(COOCH₃)₂ electrolyte. As shown in Fig. 6b, the peak power density of KJ-Co-H was about 135 mW/cm², much higher than 105 mW/cm² of KJ-Co-M. Moreover, the peak power density of KJ-Co-H was also 25 mW/cm² higher than that of Pt/C–Ir/C-based full cell. With respect to the polarization curve, the potential hysteresis of KJ-Co-H was merely 1.8 V at the current density of 125 mA/cm² during the cell charge/discharge. Compared with KJ-Co-H, this value increased to 2.06 V for KJ-Co-M and 2.15 V for Pt/C–Ir/C. Furthermore, the long cycling test was conducted at a current density of 30 mA/cm² with 20 min' discharge and 20 min' charge. Compared with the lifetime of 21 h for Pt/C–Ir/C and 150 h for KJ-Co-M, KJ-Co-H possessed the most durable cyclability without significant voltage fading even after 450 h of operation in Fig. 6c. This impressive full-cell durability, in line with the stable ORR and OER chronoamperometric behaviors at a given constant potential as shown in Fig. 5e and f, can again be attributed to the pore confinement design. Specifically, the carbon pores prevented the agglomeration of Co nanoparticles throughout the repeated cycles, as proved by the morphology and element mapping of KJ-Co-H after 450 h' cycle in Fig. 6d and e. In contrast, KJ-Co-M and Pt/C–Ir/C lacked such structural advantages, leading to a short and deteriorated cycle life.

4. Conclusion

To consummate, carbon-pore-sheathed cobalt nanoseeds for Zn-air batteries, as a proof-of-concept, was designed by loading Co nanoparticles into N-doped defective carbon pores. As the water vapor adsorbed, the cobalt precursor simultaneously hydrolyzed in the carbon pores, and subsequently transformed into Co nanoparticles after the heat treatment in ammonia. Concurrently, the carbon host was trimmed by the carbothermic reduction of the Co hydrolysis product and nitridation process, resulting in enlarged pore volumes and increased surface areas. The high electronic conductivity from metallic Co nanoparticles and facile electrolyte/gas diffusion within the well-tuned porous carbon structure, forms the prerequisite, three-phase boundary for an exceptional catalyst. Moreover, the synergic effect from the N-doping, Co–N–C bond and graphitic/graphenic carbon defects, introduced from the nitridation and carbothermic reaction, further boosted the catalytic activity. Most importantly, the prevalent dilemma with nanomaterial instability did not surface in this unique catalyst design. This merit should be attributed to the agglomeration prevention due to the carbon pore confinement effect. This agglomeration was prevented not only in the carbothermic reactions during the synthesis, but also in the long cycling battery test. By meticulously balancing the high catalytic activity and stable cyclability, this unique catalyst

delivered an excellent Zn air battery performance. Specifically, a high ORR half-wave potential of 0.847 V and a low OER potential at 10 mA/cm² of 1.593 V were delivered, which was among the outstanding bifunctional catalysts. In addition, the full cell delivers a peak power density of 135 mW/cm² at a current density of 200 mA/cm², and a 450 h stable cycling performance without fading at a current density of 30 mA/cm². Lastly, this carbon-pore loading design possesses the feasibility for a greater potential implementation in areas of battery and adsorption beyond electrochemical catalysis.

Acknowledgements

Z. Chen expresses the appreciation to the University of Waterloo, Natural Sciences and Engineering Research Council of Canada (NSERC) and the Waterloo Institute for Nanotechnology for their financial support. Z. Chen also gratefully acknowledges the Canadian Center for Electron Microscopy (CCEM) at McMaster University for TEM and EELS characterization. Part of electron microscopy work was performed at the Center for Functional Nanomaterials, Brookhaven National Laboratory, which is supported by the U.S. Department of Energy, Office of Basic Energy Science, under contract No. DE-SC0012704. J. Lu gratefully acknowledges support from the U.S. Department of Energy, Office of Energy Efficiency and Renewable Energy, Vehicle Technologies Office. Argonne National Laboratory is operated for DOE Office of Science by UChicago Argonne, LLC, under contract number DE-AC02-06CH11357.

Appendix A. Supplementary data

Supplementary data to this article can be found online at <https://doi.org/10.1016/j.nanoen.2019.104051>.

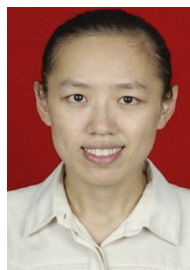
References

- [1] S.P. Jiang, *Mater. Sci. Eng. A* 418 (2006) 199–210.
- [2] C. Xu, H. Wang, P.K. Shen, S.P. Jiang, *Adv. Mater.* 19 (2007) 4256–4259.
- [3] Z. Xing, S. Wang, A. Yu, Z. Chen, *Nano Energy* 50 (2018) 229–244.
- [4] Z. Luo, L. Liu, J. Ning, K. Lei, Y. Lu, F. Li, J. Chen, *Angew. Chem. Int. Ed.* 57 (2018) 9443–9446.
- [5] S. Jin, Y. Jiang, H. Ji, Y. Yu, *Adv. Mater.* (2018) 1802014.
- [6] Z. Wang, L. Zhou, X.W. Lou, *Adv. Mater.* 24 (2012) 1903–1911.
- [7] J. Jiang, Y. Li, J. Liu, X. Huang, C. Yuan, X.W. Lou, *Adv. Mater.* 24 (2012) 5166–5180.
- [8] H. Kim, B. Han, J. Choo, J. Cho, *Angew. Chem.* 120 (2008) 10305–10308.
- [9] N.S. Choi, Z. Chen, S.A. Freunberger, X. Ji, Y.K. Sun, K. Amine, G. Yushin, L.F. Nazar, J. Cho, P.G. Bruce, *Angew. Chem. Int. Ed.* 51 (2012) 9994–10024.
- [10] Z.P. Cano, D. Banham, S. Ye, A. Hintennach, J. Lu, M. Fowler, Z. Chen, *Nature Energy* 3 (2018) 279.
- [11] Z. Xing, X. Luo, Y. Qi, W.F. Stickler, K. Amine, J. Lu, X. Ji, *Chem. Nano. Mat* 2 (2016) 692–697.
- [12] J.S. Lee, S. Tai Kim, R. Cao, N.S. Choi, M. Liu, K.T. Lee, J. Cho, *Adv Energy Mater* 1 (2011) 34–50.
- [13] I.S. Amiinu, X. Liu, Z. Pu, W. Li, Q. Li, J. Zhang, H. Tang, H. Zhang, S. Mu, *Adv. Funct. Mater.* 28 (2018) 1704638.
- [14] X. Wang, Y. Li, T. Jin, J. Meng, L. Jiao, M. Zhu, J. Chen, *Nano Lett.* 17 (2017) 7989–7994.
- [15] J. Fu, Z.P. Cano, M.G. Park, A. Yu, M. Fowler, Z. Chen, *Adv. Mater.* 29 (2017) 1604685.
- [16] Z. Chen, M. Waje, W. Li, Y. Yan, *Angew. Chem.* 119 (2007) 4138–4141.
- [17] W. Zang, A. Sumboja, Y. Ma, H. Zhang, Y. Wu, S. Wu, H. Wu, Z. Liu, C. Guan, J. Wang, *ACS Catal.* 8 (2018) 8961–8969.
- [18] Y.-N. Chen, Y. Guo, H. Cui, Z. Xie, X. Zhang, J. Wei, Z. Zhou, *J. Mater. Chem.* 6 (2018) 9716–9722.
- [19] H.B. Yang, J. Miao, S.-F. Hung, J. Chen, H.B. Tao, X. Wang, L. Zhang, R. Chen, J. Gao, H.M. Chen, *Science advances* 2 (2016) e1501122.
- [20] X.F. Lu, Y. Chen, S. Wang, S. Gao, X.W. Lou, *Adv. Mater.* (2019) 1902339.
- [21] J. Fu, Z.P. Cano, M.G. Park, A. Yu, M. Fowler, Z. Chen, *Adv. Mater.* 29 (2017).
- [22] Z. Liu, Z. Zhao, Y. Wang, S. Dou, D. Yan, D. Liu, Z. Xia, S. Wang, *Adv. Mater.* 29 (2017) 1606207.
- [23] D. Yan, Y. Li, J. Huo, R. Chen, L. Dai, S. Wang, *Adv. Mater.* 29 (2017) 1606459.
- [24] H. Osgood, S.V. Devaguptapu, H. Xu, J. Cho, G. Wu, *Nano Today* 11 (2016) 601–625.
- [25] C. Tang, H.S. Wang, H.F. Wang, Q. Zhang, G.L. Tian, J.Q. Nie, F. Wei, *Adv. Mater.* 27 (2015) 4516–4522.
- [26] G. Wu, K.L. More, C.M. Johnston, P. Zelenay, *Science* 332 (2011) 443–447.

- [27] W. Xia, A. Mahmood, Z. Liang, R. Zou, S. Guo, *Angew. Chem. Int. Ed.* 55 (2016) 2650–2676.
- [28] W. Wang, F. Lv, B. Lei, S. Wan, M. Luo, S. Guo, *Adv. Mater.* 28 (2016) 10117–10141.
- [29] R. Lv, T. Cui, M.S. Jun, Q. Zhang, A. Cao, D.S. Su, Z. Zhang, S.H. Yoon, J. Miyawaki, I. Mochida, *Adv. Funct. Mater.* 21 (2011) 999–1006.
- [30] D.P. Leonard, W.F. Stickle, X. Ji, *ACS Appl. Energy Mater.* 1 (2018) 3593–3597.
- [31] Y. Han, Y.-G. Wang, W. Chen, R. Xu, L. Zheng, J. Zhang, J. Luo, R.-A. Shen, Y. Zhu, W.-C. Cheong, C. Chen, Q. Peng, D. Wang, Y. Li, *J. Am. Chem. Soc.* 139 (2017) 17269–17272.
- [32] B.Y. Guan, L. Yu, X.W. Lou, *Advanced Science* 4 (2017) 1700247.
- [33] S. Gadipelli, T. Zhao, S.A. Shevlin, Z. Guo, *Energy Environ. Sci.* 9 (2016) 1661–1667.
- [34] Z. Xing, N. Gao, Y. Qi, X. Ji, H. Liu, *Carbon* 115 (2017) 271–278.
- [35] Y. Shen, *J. Mater. Chem.* 3 (2015) 13114–13188.
- [36] Z. Xing, B. Wang, J.K. Halsted, R. Subashchandrabose, W.F. Stickle, X. Ji, *Chem. Commun.* 51 (2015) 1969–1971.
- [37] Z. Xing, Y. Qi, Z. Tian, J. Xu, Y. Yuan, C. Bommier, J. Lu, W. Tong, D.-e. Jiang, X. Ji, *Chem. Mater.* 29 (2017) 7288–7295.
- [38] L. Cançado, K. Takai, T. Enoki, M. Endo, Y. Kim, H. Mizusaki, A. Jorio, L. Coelho, R. Magalhaes-Paniago, M. Pimenta, *Appl. Phys. Lett.* 88 (2006) 163106.
- [39] Z. Xing, G. Li, S. Sy, Z. Chen, *Nano Energy* 54 (2018) 1–9.
- [40] S. Kundu, T.C. Nagaiah, W. Xia, Y. Wang, S.V. Dommele, J.H. Bitter, M. Santa, G. Grundmeier, M. Bron, W. Schuhmann, *J. Phys. Chem. C* 113 (2009) 14302–14310.
- [41] Y. Guo, P. Yuan, J. Zhang, Y. Hu, I.S. Amiinu, X. Wang, J. Zhou, H. Xia, Z. Song, Q. Xu, *ACS Nano* 12 (2018) 1894–1901.
- [42] J.K. Nørskov, J. Rossmeisl, A. Logadottir, L. Lindqvist, J.R. Kitchin, T. Bligaard, H. Jonsson, *J. Phys. Chem. B* 108 (2004) 17886–17892.



Guoqiang Tan is a Professor in the School of Materials Science and Engineering at Beijing Institute of Technology (BIT). He received his B.S. from Hunan University in 2007, and Ph.D. from BIT in 2014. He then worked as a postdoc at Argonne National Laboratory (2014–2018) and at University of California, Los Angeles (2018–2019). His research interests focus on advanced materials and battery configurations for high energy rechargeable battery systems.



Dr. Aiju Li is a professor in School of Chemistry and Environment, South China Normal University. Her research interests are in advanced lead based grids-alloys for lead-acid batteries and additives for the electrolyte of lithium-ion batteries.



Jingde Li is an Associate Professor in School of Chemical Engineering and Technology at Hebei University of Technology. He received his Ph.D. degree in Chemical Engineering from University of Waterloo in 2014 under the supervision of Prof. Eric Croiset and Prof. Luis Ricardez-Sandoval. Before he joined Hebei University of Technology, he works as a postdoctoral fellow with Prof. Zhongwei Chen and Prof. Eric Croiset at University of Waterloo. His research focuses on multi-scale simulation (e.g. DFT, KMC, FEA) on heterogeneous catalysis process and development of energy conversion and storage materials.



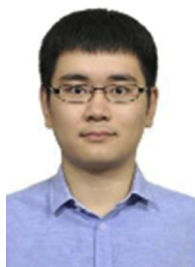
Yue Niu graduated with B.A.Sc. in the Department of Chemical Engineering and Technology from Tianjin University in 2017. Currently, he is working on his M.A.Sc. with Prof. Zhongwei Chen at the University of Waterloo. His research focuses on non-precious metal catalysts, especially single atom catalysts for electrochemical applications such as fuel cells and zinc-air batteries.



Na Li is a Ph.D student in Frontier Institute of Science and Technology jointly with College of Science at Xi'an Jiaotong University under the supervision of Prof. Yaping Du. She studied at Brookhaven National Lab as an exchange student in Dr. Dong Su's group during 09/2017-12/2018. Her research mainly includes the synthesis of nanomaterials and structural characterization of the nano-sized transition metal compounds for secondary ion batteries.



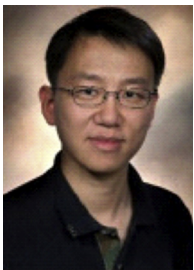
Zhenyu Xing graduated with B.Sc. of chemistry from Jilin University in 2012. He earned his Ph.D. in chemistry from Oregon State University in 2016 under the supervision of Prof. Xiulei Ji. He did his Postdoc research with Prof. Zhongwei Chen at University of Waterloo since 2017. Currently, he is an Associate Professor in Department of Chemistry at South China Normal University. His research focuses on preparation, structure, property and application of porous carbon materials.



Ya-Ping Deng received his Master's degree (2016) in Xiamen University with Prof. Shi-Gang Sun. He is now pursuing his Ph.D. in Chemical Engineering under the supervision of Prof. Zhongwei Chen at University of Waterloo. His research is currently focused on the exploration of novel electrode materials and solid-state electrolytes for lithium-ion batteries and rechargeable metal-air batteries.



Serubbabel Sy graduated with a B.A.Sc. in Chemical Engineering from University of Waterloo in 2012. He worked for a year at Syngenta, before returning to completing his M.A.Sc. also in Chemical Engineering from University of Waterloo in 2015 under the supervision of Prof. Aiping Yu. Currently, he is working on his Ph.D. with Prof. Aiping Yu and Prof Zhongwei Chen at the University of Waterloo. His research focus is on the preparation, structural design and properties of graphene materials for the use in energy related applications.



Dong Su is a staff scientist and the group leader of electron microscopy in the Center for Functional Nanomaterials, Brookhaven National Laboratory, and an adjunct professor in the Materials Science and Engineering Department, Stony Brook University. His areas of research include the electron microscopy characterization of nanosized functional materials for energy applications, and developing advanced electron microscopy techniques.



Dr. Jun Lu current is a DOE-EERE postdoctoral fellow under Vehicles Technology Program. His research interests focus on the electrochemical energy storage and conversion technology, with main focus on beyond Li-ion battery technology. Dr. Lu earned his bachelor degree in Chemistry Physics from University of Science and Technology of China (USTC) in 2000. He completed his Ph.D. from the Department of Metallurgical Engineering at University of Utah in 2009 with a major research on metal hydrides for reversible hydrogen storage application. Dr. Lu has authored/co-authored more than 70 peer-reviewed research articles and has filed over dozen patents and patent applications.



Dr. Zhongwei Chen is Canada Research Chair Professor in Advanced Materials for Clean Energy at University of Waterloo. His research interests are in the development of advanced energy materials for metal-air batteries, lithium-ion batteries and fuel cells. He has published 1 book, 7 book chapters and more than 250 peer reviewed journal articles with over 20 000 citations with H-index 70 (Google Scholar). He is also listed as inventor on 20 US/international patents, with several licensed to companies in USA and Canada. He was recipient of the 2016 E. W. R Steacie Memorial Fellowship, which followed shortly upon several other prestigious honors, including the Ontario Early Researcher Award, an NSERC Discovery Supplement Award, the Distinguished Performance and the Research Excellence Awards from the University of Waterloo.